Nanoscale Chemical Imaging of Amyloid Fibrils in Water Using Total-Internal-Reflection Tip-Enhanced Raman Spectroscopy

Yuhan Huang, Gary S Cooney, David Talaga, Renaud A. L. Vallée, Rossana Quinzi, Laurent Bouffier, Sophie Lecomte, Sébastien Bonhommeau

Nanoscale Chemical Imaging of Amyloid Fibrils in Water Using Total-Internal-Reflection Tip-Enhanced Raman Spectroscopy

Yuhan Huang,[†] Gary S. Cooney,[†] David Talaga,[†] Renaud A. L. Vallée,[‡] Rossana Quinzi,[†] Laurent Bouffier,[†] Sophie Lecomte,[§] and Sébastien Bonhommeau[†]*

[†]Univ. Bordeaux, CNRS, Bordeaux INP, ISM, UMR 5255, F-33400 Talence, France

[‡]Univ. Bordeaux, CNRS, CRPP, UMR 5031, F-33600 Pessac, France

[§]Univ. Bordeaux, CNRS, Bordeaux INP, CBMN, UMR 5248, F-33600 Pessac, France

Corresponding author

Sébastien Bonhommeau - Univ. Bordeaux, CNRS, Bordeaux INP, ISM, UMR 5255, F-33400 Talence, France ; orcid.org/0000-0002-9213-7201; Email : sebastien.bonhommeau@u-bordeaux.fr

ABSTRACT Total-internal-reflection tip-enhanced Raman spectroscopy (TIR-TERS) imaging of amyloid-β (Aβ$_{1-42}$-L34T) fibrils is performed with nanoscale spatial resolution in water, using TERS tips fabricated by bipolar electrodeposition. Ideal experimental parameters are corroborated by both theoretical simulations and TIR-TERS measurements. TIR-TERS imaging reveals the predominant parallel β-sheet secondary structure of Aβ$_{1-42}$-L34T fibrils, as well as the nanoscale spatial distribution of tyrosine, histidine and phenylalanine aromatic amino acids. Their proportion in TERS spectra can be qualitatively explained by the combined effect of their localization in the Aβ$_{1-42}$-L34T fibril structure and their molecular orientation with respect to the excitation laser light polarization. Conclusions drawn from the TERS experiments in water corroborate and significantly enrich our previous study in ambient air, thus confirming that hydration has only a marginal impact on the structure of such amyloid fibrils. This first TIR-TERS study in liquid opens fascinating perspectives for future applications in biology.

TOC GRAPHICS
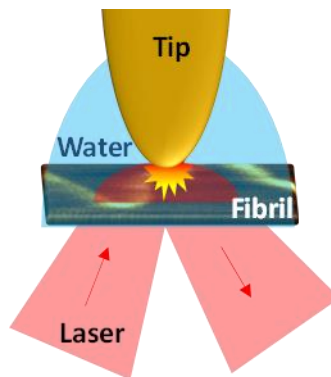
KEYWORDS Tip-enhanced Raman imaging. Total internal reflection. Localized surface plasmon resonance. Amyloid fibrils. Aromatic amino acid residues. Aqueous medium.

TEXT

Tip-enhanced Raman spectroscopy (TERS) is recognized as a powerful technique for colocalized nanoscale chemical, and structural imaging of molecules, nanomaterials and surfaces.[1,2] In TERS, the localized surface plasmon resonance (LSPR) of a noble metal tip is excited, which generates an enhanced and confined electromagnetic field at the tip apex. Scanning this optical nanosource over a sample allows Raman maps to be collected with high spatial resolution, down to the subnanometer scale.[3] Although the vast majority of TERS studies are still performed in ambient air, they can also be recorded under ultra-high vacuum conditions, in solutions and in electrochemical environments, albeit with various technical and operational constraints.[4] TERS in liquids has been suggested as a promising technique for applications in biology and medicine in 2009,[5] but its development really began six years later.[6] So far, TERS has been mostly employed in liquid media for the characterization of model systems with high Raman cross section such as self-assembled monolayers of thiols, dyes, phthalocyanine and polymer compounds, or carbon nanomaterials.[6] Very few studies showed the capacity of TERS to probe biomolecules in water,[7,8] and only one has demonstrated the ability to perform TERS imaging.[8] In the latter case, the secondary structure of amyloid-β (Aβ) fibrils, protofibrils and oligomers, which are peptide assemblies that are known to be implicated in Alzheimer's disease, was examined to identify differences between these amyloid aggregates. Similar investigations were previously accomplished in ambient air on Aβ$_{1-42}$ fibrils and oligomers.[9] Additionally, recent reports on tau fibrils formed in the presence of phospholipids and RNA cofactors, which are implicated in neurodegenerative disorders, have been published.[10,11] Apart from the interest aroused by the possible better understanding of their biological activity, amyloid fibrils constitute highly relevant objects for TERS studies owing to their nanoscale composition and structural heterogeneity. They

are known to show nanoscale hydrophobic, hydrophilic, and mixed domains depending on their amino acid content.[12,13]

Herein, we present the TERS imaging in water of long amyloid fibrils formed by self-aggregation of a mutant Aβ$_{1-42}$ peptide in which a single leucine (L) amino acid has been replaced by a threonine (T) at position 34 in the wild-type peptide sequence. This Aβ$_{1-42}$-L34T peptide has the property of forming fibrils very rapidly, and these fibrils have been shown to be less toxic than harmful Aβ fibrils implicated in Alzheimer's disease.[14] Aβ$_{1-42}$-L34T fibrils have been previously characterized by TERS, which highlighted their parallel β-sheet secondary structure,[9] but imaging was not undertaken at that time, neither in ambient air nor in liquid. Furthermore, very little information was reported on the amino acid content.[9] In the current study, TERS experiments have been carried out using an original TERS system in total internal reflection (TIR), which combines atomic force microscopy (AFM) and Raman spectroscopy. This experimental configuration turned out to be more efficient than classical bottom-illumination geometries using linearly or radially polarized laser light, especially for TERS imaging of biomolecules such as amyloid-like fibrils.[11,15,16] To the best of our knowledge, this work is the first report of TIR-TERS experiments performed on non-resonant biomolecules in liquid. Furthermore, these experiments are conducted in a non-gap mode configuration, for which L34T fibrils were simply deposited on a glass substrate, rather than on a noble metal one.[17] This limits the electromagnetic enhancement of the Raman signature of the sample, but increases the scope of the results.

Figure 1 presents two-dimensional (2D) finite-difference time-domain (FDTD) simulations considering parameters consistent with experimental ones. A TERS tip with nanoscale roughness is considered, which accounts for the fact that the high lateral spatial resolution and the TERS

enhancement are not directly driven by the apex diameter of metallized AFM tips, as frequently observed in TERS experiments (Figure 1A).[3,9-11] In fact, they are rather linked to the presence of nanoscale gold protrusions at the tip end.[18] For a TERS tip with a 60 nm-large apex, the extinction cross section is dominated by the scattering contribution, which is also significantly red shifted by 88 nm in water with respect to air, as a consequence of the dielectric screening effect of gold charges in water (Figure 1B).[19-21] This remains true for larger tip apexes, but the scattering cross section is then even more red shifted and significantly broadens on the high wavelength side (Figure 2A). In the simple model considering the excitation of a dipolar LSP at the tip end, the increased apex size is indeed expected to increase the charge separation, and thus lead to a lower restoring force for the plasmon dipole oscillation, a lower frequency for the collective oscillation of electrons and a red shift of the corresponding LSPR wavelength.[22] This proves the relevance of laser irradiation at 660 nm to excite the LSPR of TERS tips immersed in water. In TIR configuration, the angle of incidence resulting in the highest electromagnetic field intensity enhancement is about 43° in air and 64°-66° in water (Figures 1C-F). Under such optimized illumination conditions, the electromagnetic field is highly confined in a 1-5 nm large region (Figure S1 in supporting information (SI)). If integrating electric fields over a 5 nm × 2 nm area below the tip, the excitation enhancement factor $\left|\frac{E}{E_0}\right|^4$ reaches 7×10^2 in air and 2×10^2 in water (Figure 1F). The decreased electromagnetic enhancement in water is in accordance with previous experimental reports on TERS of polystyrene thin films, where a reduction of TERS intensities by a factor 8 was observed in water with respect to ambient air.[19] Despite this drawback, experiments in liquid show the noticeable advantage of lowering heating effects at the tip end,[8,19] which constitutes a major asset to preserve the sample integrity upon TERS imaging. Optimal parameters

deduced from FDTD calculations (660 nm excitation wavelength and 64-66° angle of incidence) have been considered for the following TIR-TERS measurements in water.

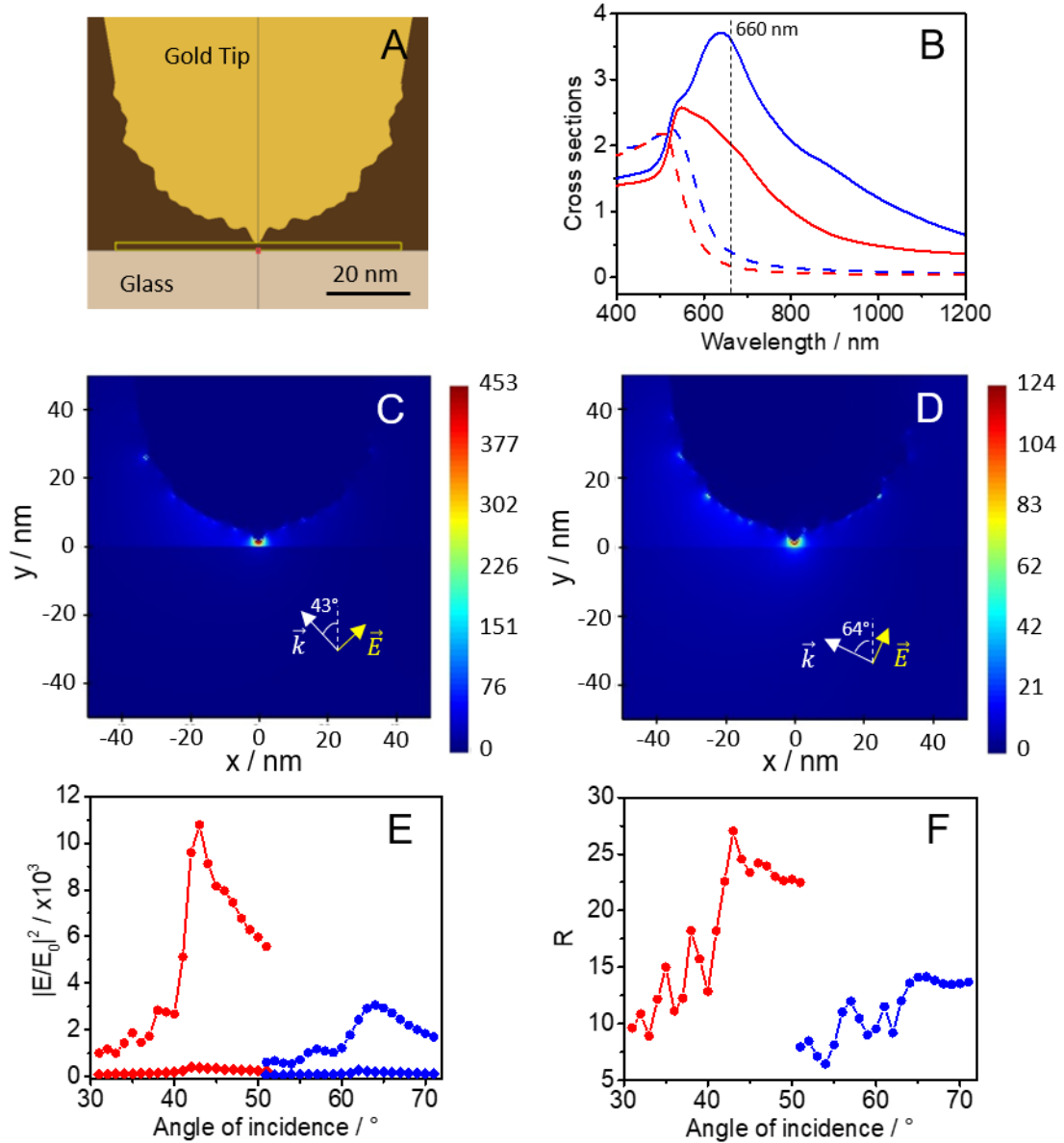**Figure 1.** (A) Geometric arrangement for 2D-FDTD calculations, with a rough gold tip at 2 nm distance from the glass surface. (B) Absorption (dashed lines) and scattering (solid lines) cross sections of the gold tip in air (red) and in water (blue). (C-D) FDTD spatial distribution of the electric field intensity enhancement $|E/E_0|^2$ when the gold tip is positioned 2 nm above the interface

with glass, for a 660 nm light excitation in TIR, and a 43° angle of incidence in air (C) or a 64° angle of incidence in water (D). Directions of $\vec{k}$ and $\vec{E}$ associated with the incident *p*-polarized light excitation are indicated. (E) Integrated electric field intensities $|E/E_0|^2$ as a function of the angle of incidence, for the gold tip retracted (diamonds) and engaged 2 nm above the glass substrate (circles) in air (red) and in water (blue). The integration of the normalized electric field intensities was carried out over the entire 5 nm × 2 nm area displayed in Figure S1. (F) Corresponding ratio R = $|E/E_0|^2_{\text{tip engaged}}/|E/E_0|^2_{\text{tip retracted}}$ as a function of the angle of incidence in air (red) and in water (blue).

TERS tips were prepared by gold bipolar electrodeposition on AFM probes. This original method will be described in details elsewhere. For TERS measurements in liquid, the electrodeposition time was set at 5 s and the applied electric field was increased compared to the requirement in air (8.1 V/cm instead of 6.9 V/cm). This was done in order to thicken the gold layer on the backside of the cantilever, and thus to better reflect the infrared (IR) AFM laser light (1300 nm) through the water which strongly absorbs in the IR range (Figure 2D). This deposition led to a 430 nm-diameter apex TERS tip (Figure 2C) and a red shift of the corresponding LSPR with values above 700 nm typically. TERS tips with LSPR bands centered below 730 nm were the most convenient for our TERS experiments under 660 nm excitation. Figure 2B shows the background of the three TERS maps of Figure 3 that will be discussed below. The maxima of these backgrounds have been shown to coincide with the LSPR of the excited metal nanostructure.[23,24] In these three cases, the maxima are centered at 1087, 1273, and 1296 cm⁻¹, which correspond to LSPR band maxima at 711, 721, and 722 nm, respectively. It is worth mentioning that TERS maps 1 and 2 have been collected using the same TERS tip, while another tip has been used for map 3 (Figures 3 C-E). This explains the similarity of the background maximum for the mean TERS spectra of maps 1 and 2. The

maximum wavelengths and the broadening of map backgrounds are in good qualitative agreement with those of the scattering signal showing an overall red shift as the tip apex diameters increase (Figure 2A). Additionally, they are self-consistent with observations on other gold-coated TERS tips prepared by potentiostatic electrodeposition,[25] and on noble metal nanoparticles.[22]
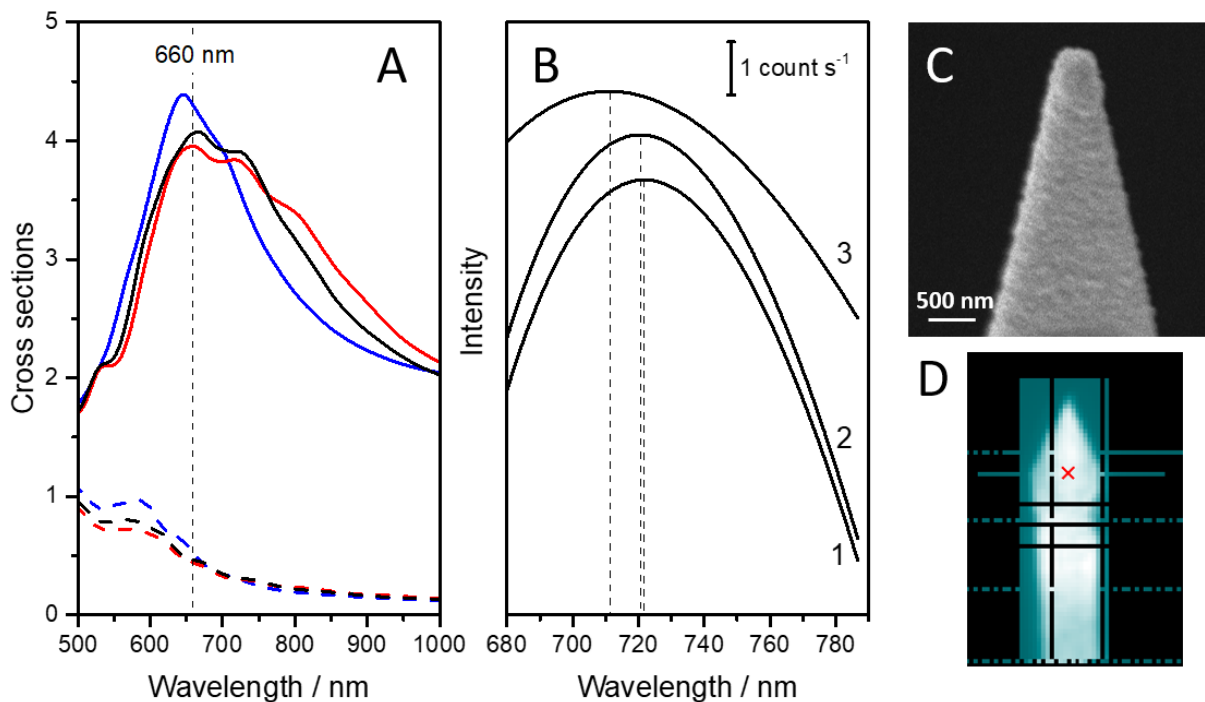

Figure 2. (A) 2D-FDTD absorption (dashed lines) and scattering (solid lines) cross sections of the gold tip in water for 180 nm (blue), 215 nm (black), and 240 nm (red) tip apex diameters. (B) Spectral backgrounds of mean TERS spectra corresponding to TERS maps labeled 1, 2, and 3 in Figure 3. (C) SEM image of the apex of a typical TERS tip used in the current study. (D) Optical image of the light reflected by the backside of a gold-coated cantilever of the same TERS tip. The white color indicates an intense reflectivity signal. The red cross locates the position where the AFM laser spot hits the cantilever to perform AFM (and TERS) imaging.

Using uncoated AFM tips, topographic tapping-mode AFM images have been performed in air to confirm the presence of $A\beta_{1-42}$-L34T fibrils at the sample surface (Figure S2). In water, it is also possible to clearly observe long fibrils using TERS tips fabricated by bipolar electrodeposition (Figure S3). Nevertheless, fibril fragments and bundles are sometimes more difficult to identify, mainly due to the degraded AFM lateral spatial resolution with large-apex-size TERS tips (Figure S3). Furthermore, it is worth mentioning that the TERS tips employed here for measurements in liquid can be also used in air provided that the laser excitation wavelength is shifted to lower values (Figure S4). As previously mentioned, this change is necessary to account for the blue shift of the LSPR upon decreasing the refractive index of the surrounding medium (from 1.33 in water to 1 in air) owing to the decreased dielectric screening of charges (Figure 1B).[20,21] However, the following discussions will only focus on experiments in water.

TERS maps of three regions of $A\beta_{1-42}$-L34T fibrils probed with two different TERS tips in water are provided in Figure 3. These maps have been plotted using a binarization procedure consisting in determining the presence or absence of specific marker bands irrespective of their intensity, provided that it is higher than three times the standard deviation of noise. This procedure has been shown to ease the interpretation of TERS maps, at least for the study of amyloid-like species.[11] AFM images of $A\beta_{1-42}$-L34T fibrils show that their height can be as low as 3 – 4 nm and reach up to 15 – 20 nm (Figures 3A, S2, and S3). As they are known to look like twisted filiform structures rather than ribbon-like ones (Figure S2),[9,14,26] their height is a good indication of their diameter. AFM and TERS images have been collected using the same TERS tips, namely tips with ~ 400 nm apex diameters. This explains the limited lateral spatial resolution of AFM images due to tip-sample convolution effects (~ 140 nm, Figure S3), and the significant lateral thickness of $A\beta_{1-42}$-L34T fibrils suggested by AFM imaging. In TERS maps however, the lateral spatial resolution is

improved and reaches ~ 50 nm (Figures 3, 4, and S4), which is consistent with previous TERS imaging experiments on comparable fibril samples in liquid medium.[8]

The parallel β-sheet secondary structure of L34T fibrils can be identified in the spectral region assigned to amide I bands (1620 – 1630 cm^{-1}).[8] The intensity integration of marker bands in this spectral range leads to TERS maps revealing a very good colocalization of parallel β-sheets and Aβ$_{1-42}$-L34T fibrils on the AFM image (Figures 3C, 3D and 3E), as expected for these fibrils.[9,14] Amide I bands were rarely observed in the 1660 – 1680 cm^{-1} region attributed to the fibril core and anti-parallel β-sheets, which confirms the absence of these latter secondary structures, and indicates that our TERS tips mainly excited a 1 – 2 nm sample thickness, as reported for TERS studies on other biological specimens.[8,16,27] In dry conditions, N- and C-terminal Aβ$_{1-42}$-L34T peptide regions should lie directly on the fibril core in a disordered way, which is not the case in aqueous environment. While raster scanning an amyloid fibril, a TERS tip may encounter nanoscale areas with naked fibril core in air, which should be less probable in water, thus leading to an easier detection of the amyloid fibril core in air than in water. In addition, parallel β-sheet secondary structures can usually be identified by investigating the spectral region assigned to amide III bands (1220 – 1230 cm^{-1}).[8,9,28] However, TERS map pixels with potential contribution of parallel β-sheets were overrepresented on the basis of spectral analysis limited to amide III bands, compared to observations focusing on the study of amide I bands (Figures S5 and S8). This is likely due to the presence of additional spectral contributions in the amide III band region, such as those of CH bending and CC stretching vibrations of amino acids.[28] This overrepresentation of amide III bands is globally consistent with TERS experiments in air, in which amide I bands were even sometimes absent in TERS spectra of amyloid fibrils.[29]
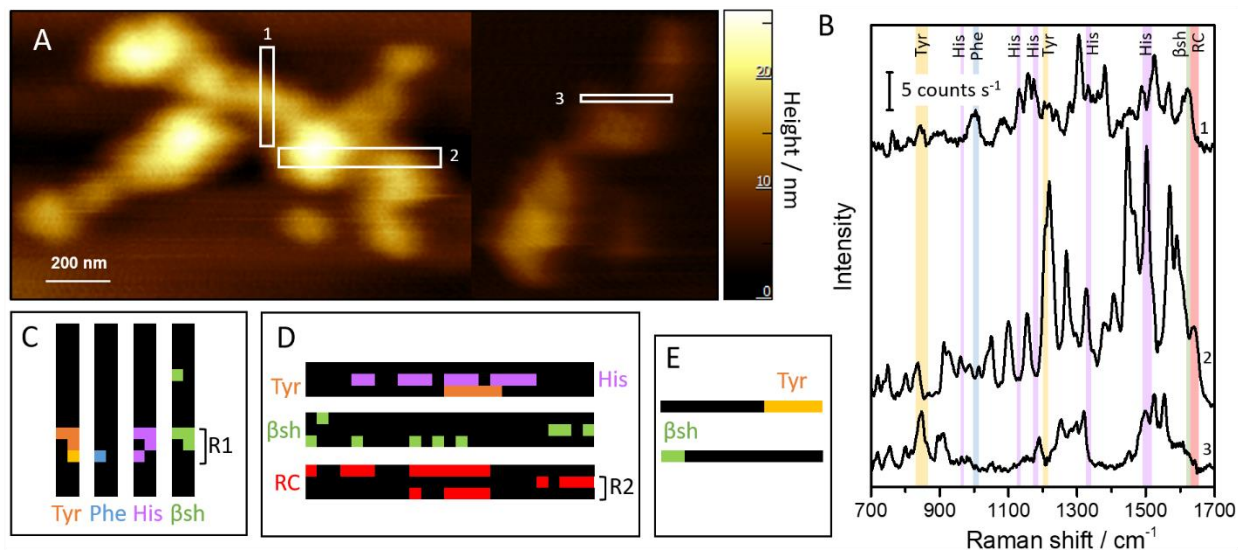
Figure 3. (A) Tapping-mode topographic AFM image of Aβ$_{1-42}$-L34T fibrils. (B) Mean TERS spectra determined in sample areas delimited by white boxes labeled 1, 2, and 3 in A, by spectral averaging over the R1 (3 lines, 6 pixels) and R2 (2 lines, 50 pixels) regions indicated in C and D for boxes 1 and 2, and over the whole box 3 (1 line, 14 pixels). TERS spectra used to calculate these mean spectra are plotted in Figures S6A, S6B, and S7. (C-E) Binarized TERS maps showing the spatial distribution of amino acids (Tyr, Phe, and His) as well as parallel β-sheet (βsh) and random coil (RC) secondary structures in fibril portions labeled 1 (C), 2 (D) and 3 (E). The spectral ranges considered for each vibrational mode are provided in B (Tyr: orange, Phe: blue, His: violet, βsh: green, and RC: red). For Tyr, dark and light orange colors are used when two Tyr marker bands and a single one are detected in the TERS spectrum of the corresponding image pixel, respectively. Scanning step size: 20 nm; Acquisition time: 10 s (maps 1 and 3), 5 s (map 2).

In the same vein, the presence of random coil secondary structures in Aβ$_{1-42}$-L34T fibrils could be manifested by amide I bands (1630 – 1655 cm^{-1}) and amide III bands (1240 – 1260 cm^{-1}),[8-13,28] but

spectral fingerprints are quite scarce at these wavenumbers. Figure 3D reports the spatial distribution of random coil secondary structure on a $A\beta_{1-42}$-L34T fibril portion. We can note that these structures can be observed either in the presence or in the absence of parallel β-sheets, even though this second option is more frequent. TERS bands emerging sometimes in the 1230-1240 cm^{-1} spectral range are commonly assigned to amide III bands reflecting the presence of antiparallel β-sheets.[8] However, it is unsure whether these spectral contributions are not simply linked to amino acids.[28] Moreover, there is no clear evidence of antiparallel β-sheet secondary structures in the amide I band region between 1660 and 1680 cm^{-1}, as already mentioned.[8] Finally, TERS bands which are frequent in the 1500 – 1580 cm^{-1} spectral range can be assigned to amide II bands as well as various amino acids,[8,28] thus making any interpretations based on this spectral region quite ambiguous.

Besides peptide secondary structures, different spectral signatures of amino acid residues could also be identified in TERS maps of distinct $A\beta_{1-42}$-L34T fibril portions, with good correlation with height AFM images of the probed $A\beta_{1-42}$-L34T fibrils. In Figures 3C, 3D and 3E, a specific TERS band of tyrosine (Tyr) assigned to the Tyr Fermi doublet can be distinguished at 830 – 865 cm^{-1}.[8,13,28] This band is sometimes associated with another spectral feature at 1200 – 1214 cm^{-1} attributed to the CH ring symmetric stretching of Tyr in TERS spectra (Figures 3C and 3D),[12,28] but this double-band behavior is not systematically observed (Figures 3C and 3E). As no intense vibrational band of other amino acid residues are expected in the 830 – 865 cm^{-1} spectral range, the detection of the Tyr ring breathing vibration can however be considered sufficient for confirming the presence of Tyr.[13,30,31] In the same vein, phenylalanine (Phe) can be identified by single-band assignment, thanks to its ring breathing vibration at 997 – 1014 cm^{-1}.[28] The situation is more complex for histidine (His) for which vibrational bands are less specific and could be

potentially assigned to several amino acids.[11-13,28] A reliable detection of His thus requires at least the observation of three coexisting bands at 960 – 970 cm^{-1}, 1125 – 1135 cm^{-1}, 1172 – 1186 cm^{-1}, 1323 – 1337 cm^{-1}, and/or 1490 – 1517 cm^{-1} in each TERS spectrum.[11-13] These bands can be tentatively assigned to His ring deformation, CN stretching / CH bending, NCN stretching / NH bending, CN ring stretching, and C=C asymmetric stretching / NH bending vibrations, respectively.[28] Figures 3C and 3D show the spatial distribution of His, Tyr and Phe in maps 1 and 2. No His was discerned in map 3. No Phe could be identified in maps 2 and 3. Interestingly, while the Aβ_{1-42}-L34T peptide sequence contains 1 Tyr (Tyr10), 3 His (His6, His13 and His14) and 3 Phe residues (Phe4, Phe19 and Phe20),[32] His appears just a bit more frequently than Tyr, and Phe is nearly undetectable in TERS spectra. According to Figure 3, His, Tyr and Phe residues are detected in ~ 14 %, ~ 12 % and less than 1 % of TERS spectra acquired from twisted Aβ_{1-42}-L34T fibrils. The strong difference between His, Tyr and Phe proportions and their expected abundance inside the fibrils cannot be simply related to their scattering cross sections, since these three amino acids are aromatic and all exhibit high Raman cross sections. Two reasons can explain it: i) the localization of these amino acid residues and ii) their molecular orientation. According to the cryo-electron microscopy density image of Aβ_{1-42} fibrils,[32] among the 3 His residues, His6 and His13 are thought to form salt bridges with a glutamic acid residue (Glu11). Only His14 points outside the fibril core and is thus able to be favorably probed by TERS. Similarly, two Phe residues (Phe4 and Phe19) are expected to face the fibril hydrophobic core. Only Phe20 is exposed to the fibril surface, like His14 and Tyr10. Moreover, Phe residues are known to be involved in the formation of Aβ fibrils probably due to their propensity to interact by π-π stacking in mature fibrils.[33] The same remains true for the Aβ_{1-42}-L34T fibrils for which the Phe content is exactly the same. The low proportion of Phe residues detected at the fibril surface was already reported in a previous

TERS imaging study of wild-type Aβ$_{1-42}$ fibrils in ambient air,[13] but its origin remained elusive. The position of the His and Tyr residues inside the fibril structure could mostly explain their proportions in TERS spectra, provided that the fibril surface was essentially probed by TERS. However, the sole localization argument cannot explain the marked difference with the apparent Phe content. The second parameter to consider is the molecular orientation, which is critical in TERS since the highest TERS signals are expected for vibrations parallel to the excitation laser light polarization. As shown by cryo-electron microscopy for Aβ$_{1-42}$ fibrils,[32] His6 and His13 are almost perpendicular to His14. Therefore, the three His residues cannot contribute equally to the TERS signal. In addition, Phe20 is almost oriented parallel to His14. However, while Phe4 is only slightly tilted with respect to His6 and His13, Phe19 is almost perpendicular to them. Tyr10 is oriented parallel to His6 and His13, but perpendicular to His14 and Phe20 hence.[32] The relative proportions of His, Tyr and Phe thus suggest that the molecular orientation of Tyr10 is the most favorable in our TERS experiment. As Phe and His residues parallel to Tyr10 are more buried below the surface, their contributions in TERS spectra are expected to be proportionally lower. Furthermore, only a single Phe residue (Phe4) but two His ones (His6 and His13) are approximately parallel to Tyr10, thus indicating easier detection of His with respect to Phe. These arguments converge towards a combined effect of localization and molecular orientation to explain the origin of the observed amino acid content, provided that TERS probing is not limited to the fibril surface but detect also, to some extent, the amino acids inside the fibrils. Accordingly, a fibril fragment for which the fibril core is more exposed should exhibit more frequent TERS contributions of Phe. Figure 4 shows a 3 nm-high Aβ$_{1-42}$-L34T fibril fragment characterized by TERS along a 12-pixels line. The Phe ring breathing vibration is then detected in 5 pixels, i.e. in 42 % of the TERS spectra. This high proportion of Phe relative to its counterpart in Figure 3 for

which entire fibrils were studied clearly indicates their main presence in the $A\beta_{1-42}$-L34T fibril core, and their less effective excitation in intact fibrils. We can add that no spectral contribution of core β-sheets was discerned in these latter spectra in the 1660 – 1680 cm^{-1} range, but this may be due the low intensity of such vibrational TERS bands, even in ambient air,[9,10,13] and to their unfavorable orientation with respect to the TERS tip.[2,34] More TERS experiments would be necessary to draw a definitive conclusion on this point, but this is out of the scope of the present work.
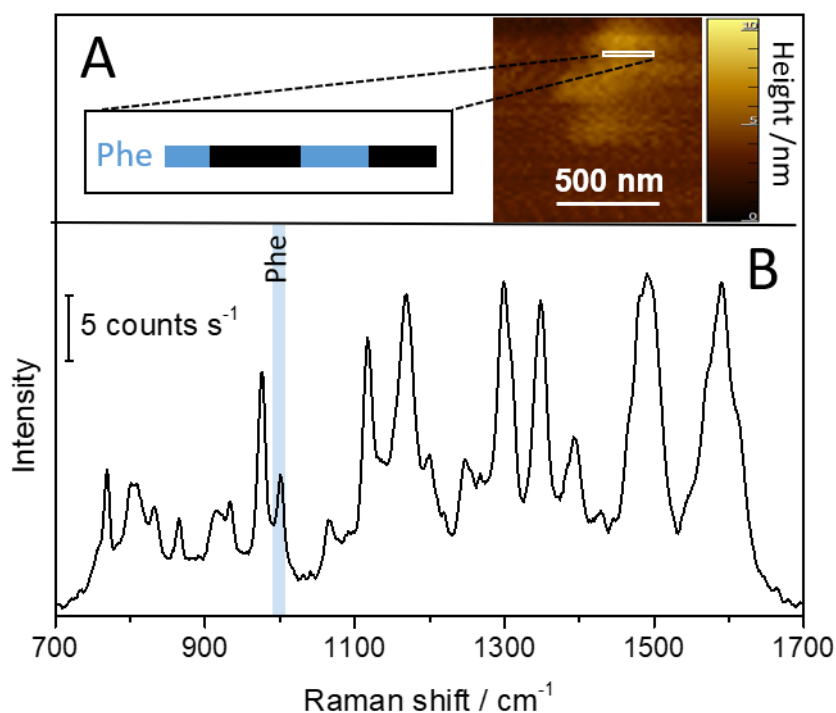

Figure 4. (A) Tapping-mode topographic AFM image of a L34T fibril fragment, and binarized TERS map showing the spatial distribution of Phe amino acids in white box (12 pixels) indicated on the AFM image. (B) Mean TERS spectrum averaged over all pixels of the white box. TERS spectra used to calculate it are plotted in Figure S6C. The blue band indicates the Phe spectral

region considered to obtain the TERS map plotted in A. Scanning step size: 20 nm; Acquisition time: 20 s.

Most of the amino acids in the Aβ$_{1-42}$ peptide, and its L34T mutant, are not aromatic. Among them, 1 arginine (Arg), 2 lysine (Lys), and 6 valine (Val) residues show TERS features, which have already been reported in TERS spectra of Aβ$_{1-42}$ fibrils in an aqueous medium,[8] but not in ambient air.[9,13] In current TERS spectra (Figures 3, 4 and S5), we observed bands assigned to Arg, Lys, and Val in relatively low proportion, irrespective of the excited fibril sample. In particular, the safe identification of Arg and Lys generally requires the observation of two coexisting TERS bands,[11,12] while only one is discerned with high enough intensity in most spectra. Therefore, as in ambient air,[9,13] the spatial distribution of non-aromatic amino acids could not be safely determined.

In summary, based on theoretical and experimental approaches, we have proven the relevance of TIR-TERS systems to perform nanoscale chemical imaging of a biological specimen in water. The investigated amyloid fibrils produced by self-assembly of Aβ$_{1-42}$-L34T peptides predominantly showed parallel β-sheet secondary structure, as well as His and Tyr amino acids, as observed in ambient air.[9] Phe residues were mainly detected in a thin Aβ$_{1-42}$-L34T fibril fragment for which the fibril core was probably more exposed, and could thus be more efficiently excited by the enhanced electromagnetic field at the TERS tip apex. The proportions of aromatic amino acid residues could be explained in view of the combined effect of their localization in the fibril structure and their molecular orientation. This enriches significantly our preceding report on Aβ$_{1-42}$-L34T fibrils, where the amino acid content was only marginally discussed.[9] The fact that the structure of amyloid fibrils is not drastically affected by hydration[35] is corroborated by our TERS experiments. Apart from the inherent interest of TERS measurements in liquid to reduce potential heating effects,[8] our study confirms the possibility to perform TIR-TERS investigations in aqueous

media, and extract valuable information in an environment more biologically-relevant than ambient air.

METHODS

Aβ$_{1-42}$-L34T peptides were selected in yeast, and produced and purified as described elsewhere.[36] Purity of the peptides was confirmed by size exclusion chromatography and mass spectrometry. After purification, Aβ$_{1-42}$-L34T monomers were frozen in liquid nitrogen and conserved at − 80°C until use. Aβ$_{1-42}$-L34T fibrils were grown by self-aggregation of monomers upon incubation for 5 days in ultrapure (Milli-Q®) water. A 4 µL aliquot of a Aβ$_{1-42}$-L34T fibril suspension diluted in Milli-Q® water (pH ~ 7) was simply drop-casted on a glass coverslip, and rinsed with Milli-Q® water after 40 min incubation, so as to prepare a sample convenient for TERS experiments.

TERS measurements were carried out on a custom TIR-TERS system. This system coupled a CombiScope AFM instrument (AIST-NT, HORIBA Scientific) and a high-resolution Raman spectrometer (LabRAM HR, HORIBA Scientific), with an inverted optical microscope (Olympus IX 71). It is equipped with a high numerical aperture oil-immersion 60× TIR objective (NA 1.49) and a 300 grooves/mm grating. Grace Bio-Labs SecureSeal™ imaging spacers (diameter × thickness: 13 mm × 0.12 mm, Merck) were used as liquid wells. They were directly glued on the sample glass substrate. TERS tips were fabricated by bipolar electrodeposition on commercial silicon AFM tips (APP-Nano, ACCESS-FM) in a gold plating bath (Metalor ECF60) during 5 s under an electric field of 8.1 V/cm. TERS spectra of samples immersed in water were acquired using 660 nm laser irradiation with *p*-polarization at a typical angle of incidence higher than 64° in TIR configuration. In these experimental conditions, a 25 µm-diameter sample region was

excited with a 3.3 mW laser power, i.e. a laser fluence as low as 6.7 µW/µm^2. Any laser-induced damage to the analyte could therefore be ruled out. AFM and TERS imaging were performed in soft-tapping mode (10 nm tip oscillation amplitude and 85% amplitude setpoint, at a ~ 27 kHz resonance frequency) in order to avoid mechanical degradations of the sample. The integration time per TERS spectrum was 5 – 20 s. The spectrometer was calibrated before each series of measurements by zeroing the Rayleigh scattering of a bare borosilicate glass coverslip. In our experimental conditions, the spectral resolution could be estimated to be ~ 4 cm^{-1}.

2D-FDTD electromagnetic simulations (Lumerical, Ansys Inc.) were performed considering a gold tip with nanoscale roughness, as expected for TERS measurements. Perfectly matched layer (PML) boundary conditions were used to gradually attenuate fields at the boundaries, and so avoid back-reflections in the system. Except for the absorption and scattering cross sections for which a broadband excitation extending from 400 to 1200 nm was used, the frequency of the light source was fixed at 660 nm and the electric field was *p*-polarized relative to the surface. The adequacy between reflectance and transmittance deduced from FDTD calculations and classical optics theory was confirmed at the glass/air and glass/water interface. Normalized electric-field density maps were calculated over a 100 nm × 100 nm region surrounding the tip at the air/glass or water/glass interfaces (with a grid size of 0.5 nm). To estimate electric field intensities ($|E/E_0|^2$) and enhancements, the electric fields were integrated over a 5 nm × 2 nm box just below the tip end (Figure S1). Electromagnetic enhancements have been calculated as the ratio R = $|E/E_0|^2_{tip\ engaged}$/$|E/E_0|^2_{tip\ retracted}$ of the electric-field intensity when the gold tip was 2 nm above a semi-infinite glass slab (n = 1.518) and fully retracted (i.e. in the absence of any tip for the calculation).

Backgrounds of mean TERS spectra were determined using a second-degree polynomial curve fitting method implemented in the Origin 2015 software. Binarized TERS maps were obtained on the basis of the calculation of standard deviations of noise using the Origin 2015 software.

ASSOCIATED CONTENT

The following files are available free of charge.

2D-FDTD electric field density of a gold tip with nanoscale roughness, Morphology of $A\beta_{1-42}$-L34T fibrils, TERS of graphene oxide in air, Additional TERS maps, TERS spectra, Verification of the absence of contamination on TERS tips. (PDF)

AUTHOR INFORMATION

Corresponding author

Sébastien Bonhommeau - Univ. Bordeaux, CNRS, Bordeaux INP, ISM, UMR 5255, F-33400 Talence, France ; orcid.org/0000-0002-9213-7201; Email : sebastien.bonhommeau@u-bordeaux.fr

Authors

Yuhan Huang - Univ. Bordeaux, CNRS, Bordeaux INP, ISM, UMR 5255, F-33400 Talence, France ; orcid.org/0000-0002-8906-8233

David Talaga - Univ. Bordeaux, CNRS, Bordeaux INP, ISM, UMR 5255, F-33400 Talence, France. orcid.org/0000-0002-3424-9790

Renaud A. L. Vallée - Univ. Bordeaux, CNRS, CRPP, UMR 5031, F-33600 Pessac, France ; orcid.org/0000-0002-6950-2637

Gary S. Cooney - Univ. Bordeaux, CNRS, Bordeaux INP, ISM, UMR 5255, F-33400 Talence, France ; ⓘD orcid.org/0000-0001-7791-4079

Rossana Quinzi - Univ. Bordeaux, CNRS, Bordeaux INP, ISM, UMR 5255, F-33400 Talence, France.

Laurent Bouffier - Univ. Bordeaux, CNRS, Bordeaux INP, ISM, UMR 5255, F-33400 Talence, France ; ⓘD orcid.org/0000-0002-0346-1254

Sophie Lecomte - Univ. Bordeaux, CNRS, Bordeaux INP, CBMN, UMR 5248, F-33600 Pessac, France ; ⓘDorcid.org/0000-0001-8310-4849

Notes

The authors declare no competing financial interests.

REFERENCES

(1) Kurouski, D.; Dazzi, A.; Zenobi, R.; Centrone, A. Infrared and Raman chemical imaging and spectroscopy at the nanoscale. *Chem. Soc. Rev.* **2020**, *49*, 3315-3347, DOI: 10.1039/c8cs00916c.

(2) Bonhommeau, S.; Cooney, G. S.; Huang, Y. Nanoscale chemical characterization of biomolecules using tip-enhanced Raman spectroscopy. *Chem. Soc. Rev.* **2022**, *51*, 2416-2430, DOI: 10.1039/d1cs01039e.

(3) Richard-Lacroix, M.; Zhang, Y.; Dong, Z.; Deckert, V. Mastering high resolution tip-enhanced Raman spectroscopy: towards a shift of perception. *Chem. Soc. Rev.* **2017**, *46*, 3922-3944, DOI: 10.1039/c7cs00203c.

(4) Pienpinijtham, P.; Kitahama, Y.; Ozaki, Y. Progress of tip-enhanced Raman scattering for the last two decades and its challenges in very recent years. *Nanoscale* **2022**, *14*, 5265-5288, DOI: 10.1039/d2nr00274d.

(5) Schmid, T.: Yeo, B.-S.; Leong, G.; Stadler, J.; Zenobi, R. Performing tip-enhanced Raman spectroscopy in liquids. *J. Raman Spectrosc.* **2009**, *40*, 1392-1399, DOI: 10.1002/jrs.2387.

(6) Britz-Grell, A. B.; Saumer, M.; Tarasov, A. Challenges and opportunities of tip-enhanced Raman spectroscopy in liquids. *J. Phys. Chem. C* **2021**, *125*, 21321-21340, DOI: 10.1021/acs.jpcc.1c05353.

(7) Nakata, A.; Nomoto, T.; Toyota, T.; Fujinami, M. Tip-enhanced Raman spectroscopy of lipid bilayers in water with an alumina- and silver-coated tungsten tip. *Anal. Sci.* **2013**, *29*, 865-869, DOI: 10.2116/analsci.29.865.

(8) Lipiec, E.; Kaderli, J.; Kobierski, J.; Riek, R.; Skirlińska-Nosek, K.; Sofińska, K.; Szymoński, M.; Zenobi, R. Nanoscale hyperspectral imaging of amyloid secondary structures in liquid. *Angew. Chem. Int. Ed.* **2021**, *60*, 4545-4550, DOI: 10.1002/anie.202010331.

(9) Bonhommeau, S.; Talaga, D.; Hunel, J.; Cullin, C., Lecomte, S. Tip-enhanced Raman spectroscopy to distinguish toxic oligomers from Aβ_{1-42} fibrils at the nanometer scale. *Angew. Chem. Int. Ed.* **2017**, *56*, 1771-1774, DOI: 10.1002/anie.201610399.

(10)   Talaga, D.; Smeralda, W.; Lescos, L.; Hunel, J.; Lepejova-Caudy, N.; Cullin, C.; Bonhommeau, S.; Lecomte, S. PIP$_2$ phospholipid-induced aggregation of tau filaments

probed by tip-enhanced Raman spectroscopy. *Angew. Chem. Int. Ed.* **2018**, *57*, 15738-15742, DOI: 10.1002/anie.201809636.

(11)   Cooney, G. S.; Talaga, D.; Ury-Thiery, V.; Fichou, Y.; Huang, Y.; Lecomte, S.; Bonhommeau, S. Chemical imaging of RNA-tau amyloid fibrils at the nanoscale using tip-enhanced Raman spectroscopy. *Angew. Chem. Int. Ed.* **2023**, *62*, e202314369, DOI: 10.1002/anie.202314369.

(12)   Deckert-Gaudig, T.; Kurouski, D.; Hedegaard, M. A. B.; Singh, P.; Lednev, I. K.; Deckert, V. Spatially resolved spectroscopic differentiation of hydrophilic and hydrophobic domains on individual insulin amyloid fibrils. *Sci. Rep.* **2016**, *6*, 33575, DOI: 10.1038/srep33575.

(13)   Zikic, B.; Bremner, A.; Talaga, D.; Lecomte, S.; Bonhommeau, S. Tip-enhanced Raman spectroscopy of Aβ(1-42) fibrils. *Chem. Phys. Lett.* **2021**, *768*, 138400, DOI: 10.1016/j.cplett.2021.138400.

(14)   Vignaud, H.; Bobo, C.; Lascu, I.; Sörgjerd, K. M.; Zako, T.; Maeda, M.; Salin, B.; Lecomte, S.; Cullin, C. A structure-toxicity study of Aβ42 reveals a new antiparallel aggregation pathway. *Plos One* **2013**, *8*, e80262, DOI: 10.1371/journal.pone.0080262.

(15)   Talaga, D.; Bremner, A.; Buffeteau, T.; Vallée, R. A. L.; Lecomte, S.; Bonhommeau, S. Total Internal Reflection Tip-Enhanced Raman Spectroscopy of Cytochrome c. *J. Phys. Chem. Lett.* **2020**, *11*, 3835-3840, DOI: 10.1021/acs.jpclett.0c00579.

(16)   Talaga, D.; Cooney, G. S.; Ury-Thiery, V.; Fichou, Y.; Huang, Y.; Lecomte, S.; Bonhommeau, S. Total internal reflection tip-enhanced Raman spectroscopy of tau fibrils. *J. Phys. Chem. B* **2022**, *126*, 5024-5032, DOI: 10.1021/acs.jpcb.2c02786.

(17)   Stadler, J.; Oswald, B.; Schmid, T.; Zenobi, R. Characterizing unusual metal substrates for gap-mode tip-enhanced Raman spectroscopy. *J. Raman Spectrosc.* **2013**, 44, 227-233. DOI: 10.1002/jrs.4169.

(18)   Trautmann, S.; Richard-Lacroix, M.; Dathe, A.; Schneidewind, H., Dellith, J.; Fritzsche, W.; Deckert, V. Plasmon response evaluation based on image-derived arbitrary nanostructures, *Nanoscale* **2018**, *10*, 9830-9839. DOI: 10.1039/c8nr02783h.

(19)   Kumar, N.; Su, W.; Veselý, M.; Weckhuysen, B. M.; Pollard, A. J.; Wain, A. J. Nanoscale chemical imaging of solid–liquid interfaces using tip-enhanced Raman spectroscopy. *Nanoscale* **2018**, *10*, 1815-1824. DOI: 10.1039/c7nr08257f.

(20)   Mahmoud, M. A.; El-Sayed, M. A. Gold Nanoframes: Very High Surface plasmon fields and excellent near-infrared sensors. *J. Am. Chem. Soc.* **2010***, 132*, 12704-12710. DOI: 10.1021/ja104532z.

(21)   Rubio, A.; Serra, L. Dielectric screening effects on the photoabsorption cross section of embedded metallic clusters. *Phys. Rev. B* **1993**, *48*, 18222-18229. DOI: 10.1103/PhysRevB.48.18222.

(22)   Rycenga, M.; Cobley, C. M.; Zeng, J.; Li, W.; Moran, C. H.; Zhang, Q.; Qin, D.; Xia, Y. Controlling the synthesis and assembly of silver nanostructures for plasmonic applications. *Chem. Rev.* **2011**, *111*, 3669–3712. DOI: 10.1021/cr100275d.

(23)   Itoh, T.; Kikkawa Y.; Biju, V.; Ishikawa, M.; Ikehata, A.; Ozaki, Y. Variations in steady-state and time-resolved background luminescence from surface-enhanced resonance Raman scattering-active single Ag nanoaggregates. *J. Phys. Chem. B*. **2006**, *110*, 21536-21544. DOI: 10.1021/jp064070p.

(24)   Pettinger, B.; Domke, K. F.; Zhang, D.; Schuster, R.; Ertl, G. Direct monitoring of plasmon resonances in a tip-surface gap of varying width. *Phys. Rev. B* **2007**, *76*, 113409. DOI: 10.1103/PhysRevB.76.113409.

(25)   Huang, Y.; Talaga, D.; Garrigue, P.; Salinas, G.; Cooney, G. S.; Reculusa, S.; Kuhn, A.; Bouffier, L.; Bonhommeau, S. Nanostructured gold-coated AFM tips generated by potentiostatic electrodeposition for tip-enhanced Raman spectroscopy. *Chem. Phys. Lett.* **2023**, *832*, 140893, DOI: 10.1016/j.cplett.2023.140893.

(26)   Feuillie, C.; Lambert, E.; Ewald, M.; Azouz, M.; Henry, S.; Marsaudon, S.; Cullin, C.; Lecomte, S.; Molinari, M. High speed AFM and nanoinfrared spectroscopy investigation of $A\beta_{1-42}$ peptide variants and their interaction with POPC/SM/Chol/GM1 model membranes. *Front. Mol. Biosci.* **2020**, *7*, 571696. DOI: 10.3389/fmolb.2020.571696.

(27)   Dou, T.; Li, Z.; Zhang, J.; Evilevitch, A.; Kurouski, D. Nanoscale structural characterization of individual viral particles using atomic force microscopy infrared spectroscopy (AFM-IR) and tip-enhanced Raman spectroscopy (TERS). *Anal. Chem.* **2020**, *92*, 11297-11304. DOI: 10.1021/acs.analchem.0c01971.

(28)   Bonhommeau, S.; Lecomte, S. Tip-enhanced Raman spectroscopy: A tool for nanoscale chemical and structural characterization of biomolecules. *Chem. Phys. Chem.* **2018**, *19,* 8-18, DOI: 10.1002/cphc.201701067.

(29)   Lipiec, E.; Perez-Guaita, D.; Kaderli, J.; Wood, B. R.; Zenobi, R. Direct nanospectroscopic verification of the amyloid aggregation pathway. *Angew. Chem. Int. Ed.* **2018**, *57*, 8519-8524. DOI: 10.1002/anie.201803234.

(30)   Kurouski, D.; Deckert-Gaudig, T.; Deckert, V.; Lednev, I. K. Structure and composition of insulin fibril surfaces probed by TERS. *J. Am. Chem. Soc.* **2012**, *134*, 13323-13329. DOI: 10.1021/ja303263y.

(31)   Kurouski, D.; Deckert-Gaudig, T.; Deckert, V.; Lednev, I. K. Surface characterization of insulin protofilaments and fibril polymorphs using tip-enhanced Raman spectroscopy (TERS). *Biophys. J.* **2014**, *106*, 263-271. DOI: 10.1016/j.bpj.2013.10.040.

(32)   Gremer, L.; Schölzel, D.; Schenk, C.; Reinartz, E.; Labahn, J.; Ravelli, R. B. G.; Tusche, M.; Lopez-Iglesias, C.; Hoyer, W.; Heise, H.; Willbold, D.; Schröder, G. F. Fibril structure of amyloid-β(1–42) by cryo–electron microscopy. *Science* **2017**, *358*, 116-119. DOI: 10.1126/science.aao2825.

(33)   Kumar, J.; Namsechi, R.; Sim, V. L. Structure-based peptide design to modulate amyloid beta aggregation and reduce cytotoxicity. *Plos One* **2015**, *10*, e0129087, DOI: 10.1371/journal.pone.0129087.

(34)   Kurouski, D.; Postiglione, T.; Deckert-Gaudig, T.; Deckert, V.; Lednev, I. K. Amide I vibrational mode suppression in surface (SERS) and tip (TERS) enhanced Raman spectra of protein specimens. *Analyst* **2013**, *138*, 1665-1673. DOI: 10.1039/c2an36478f.

(35)   Squires, A. M.; Devlin, G. L.; Gras, S. L.; Tickler, A. K.; MacPhee, C. E.; Dobson, C. M. X-ray scattering study of the effect of hydration on the cross-beta structure of amyloid fibrils. *J. Am. Chem. Soc.* **2006**, *128*, 11738-11739. DOI: 10.1021/ja063751v.

(36)   D'Angelo, F.; Vignaud, H.; Di Martino, J.; Salin, B.; Devin, A.; Cullin, C.; Marchal, C. A yeast model for amyloid-beta aggregation exemplifies the role of membrane trafficking and PICALM in cytotoxicity. *Dis. Model. Mech.* **2013**, *6*, 206-216. DOI: 10.1242/dmm.010108.